Model Predictive Control of Three-Level NPC Inverter-Fed PMSM Drives Based on a Novel Vector-Selection Scheme

Xiaomei Tang, Shuangxia Niu, *Senior Member, IEEE*, K. T. Chau, *Fellow, IEEE*, Xin Yuan, *Member, IEEE*, and W. L. Chan, *Senior Member, IEEE*

***Abstract*—Existing model predictive control (MPC) methods mostly adopt multi-vector mode to achieve better steady-state control performance. But this increases system complexity, especially for three-level inverters. In addition, various vector combinations need to be evaluated in the cost function, and cumbersome tuning of weighting factors is also involved when the common-mode voltage (CMV) and neutral point potential (NPP) imbalance issues are considered. This paper proposes a novel multi-vector-based MPC scheme to deal with these challenges. The key is to map the reference voltage vector to sub-hexagons, and the candidate region is narrowed down. Then, the dwell time of the determined voltage vectors is obtained from the cost function, which minimizes the error between the predicted reference voltage vector and the synthesis vector. In addition, the basic vectors with higher CMV amplitudes are reconstructed, and the NPP imbalance is addressed due to the employment of a hysteresis controller. Experimental results verify that the proposed method has superior performance to other multi-vector MPC algorithms.**

***Index Terms*—Common-mode voltage (CMV), model predictive control (MPC), permanent magnet synchronous motor (PMSM), three-level neutral-point-clamped (3L-NPC) inverter.**

I. Introduction

COMPARED with the traditional two-level inverter, the total harmonic distortion (THD) of the output waveform of the three-level neutral-point-clamped (3L-NPC) inverter is reduced under the same switching frequency. This is because the output voltage waveform of the three-level inverter is ladder-shaped and closer to a sine wave. At the same time, multi-level inverters also have the advantages of small voltage change rate dv/dt and minor voltage stress of power devices. Therefore, 3L-NPC is widely used in in the field of high-voltage, high-capacity, and high-accurate motor drive [1]–[3].

To make the most of the high efficiency and high power density of 3L-NPC inverter driving permanent magnet synchronous motors (PMSM), the modulations and control methods are crucial. The proportional-integral (PI) control is often adopted as the PMSM current control method for its simple structure [4], and the associated modulation method is worthwhile. The dynamic performance of the PI method is limited by the bandwidth of the internal current loop, which can be proportional to the execution time of the hardware [5]. Some nonlinear techniques, such as fuzzy control [6], neural network control [7], and sliding mode control [8], have recently emerged as effective performance improvements. Apart from these techniques, finite-set model predictive control (FS-MPC) has been widely evolved and is considered to be one of the most attractive control strategies [9]. Compared with the conventional field-oriented control and direct torque control schemes, MPC generates a switching signal directly without modulation and handles multi-objective optimization problems easily [10]–[12]. For these merits, the MPC control strategy is analyzed in this paper for 3L-NPC inverter-fed PMSM drives.

In the conventional FS-MPC introduced by Rodriguez *et al.* [13], all 27 switching actions generated by the 3L-NPC inverter are predicted by the discrete-time model in each control cycle. In the next period, the optimal voltage vector that minimizes the cost function will be applied to the control system. Therefore, FS-MPC often consumes excessive computational time and thus deteriorates system dynamic performance. Several solutions have been adopted to overcome the drawback. Zhang *et al.* [14] proposed the deadbeat-based method, which avoids predictions for 27 stator voltage or current in each control cycle. However, the computational time is still considerable when carrying out cost function calculations.

All the aforementioned methods adopt only one voltage vector in one entire control cycle, which leads to unfixed switching frequency and large current ripple. Accordingly, a dual-vector control mode is applied in [15]. It enhanced the overall inverter performance based on the current error area minimization. Xiong *et al.* constructed virtual vectors and employed a discrete time disturbance observer, which achieved good steady-state and dynamic performance [16]. Alhosaini *et al.* presented the modulation of discrete space vectors and effectively reduced the output current ripples [17]. To optimize the duty cycle for each of the 24 redivided sectors, Donoso *et al.* made use of the numerical values of cost functions [18]. However, these MPC strategies that go beyond taking a single vector have a complex vector evaluation process that also requires calculating the duration of each vector combination. To improve the computational

This work was supported in part by the the Research Grant Council of the Hong Kong Government under Projects PolyU 152109/20E and in part by RGC Collaborative Research Fund under Grant C1052-21G. (Corresponding author: Shuangxia Niu)

Xiaomei Tang, Shuangxia Niu, K. T. Chau and W. L. Chan are with the Department of Electrical and Electronic Engineering, The Hong Kong Polytechnic University, Hong Kong 999077, China (e-mail: 21040654r@connect.polyu.hk; shuangxia.niu@polyu.edu.hk; k.t.chau@polyu.edu.hk; wai-lok.chan@polyu.edu.hk).

Xin Yuan is with the School of Engineering, University of Aberdeen, AB24 3UF Aberdeen, U.K. (e-mail: xin.yuan@abdn.ac.uk).

efficiency, a preselection scheme is proposed to select the optimal vectors, and the evaluation structure is rebuilt in [19]. Two-stage optimization based on virtual VVs is employed in [20] to reduce the computation burden. In [21], the deadbeat current control principle is introduced to eliminate the iterative computations for a nine-phase open-end winding PMSM.

For a 3L-NPC inverter, operating with the unbalanced neutral point potential (NPP) will affect the reliability and lifetime of the PMSM drive system. To handle this key issue, a hexagon candidate region FS-MPC is proposed in [14], and the NPP balancing is incorporated into cost function calculation. However, the weighting factors are required to be fine tuned by trial and error, which consumes a lot of time and sacrifices the fast dynamic response. Yang *et al.* balanced the NPP by selecting proper redundant small voltage vectors [22]. The candidate voltage vectors to be evaluated are effectively reduced, and the weighting factors are eliminated as well. Yang *et al.* applied one virtual and three real vectors in one control cycle [23]. NPP balance is achieved by duration time adjustment of virtual and redundant vectors. Zhou *et al.* decoupled the control process into two stages in each control period and considered the nonlinearity of the voltage vectors caused by the unbalanced NPP [24].

Another critical issue with multi-level inverters driving electric machines is that they inherently produce a common-mode voltage (CMV). If high CMV is presented in the PMSM drive system, overvoltage stress to the winding insulation is raised, and electromagnetic interference (EMI) is generated with neighboring devices. EMI causes high-frequency overload bearing current, which needs to be suppressed to promote 3L-NPC inverter performance. The hardware increment, such as separate rectifiers and filters, will reduce overall system efficiency and increase maintenance costs. Software approaches mean eliminating CMV by modifying the control strategy. Qin *et al.* [25] divided space vectors into large, medium, and zero vectors and selected vectors corresponding to one-sixth CMV of the DC-link voltage. In [26], only the non zero vectors are applied and the dead-time effects of the inverter are considerated.

However, in the above-mentioned CMV elimination schemes, the NPP balancing is not taken into consideration. The most common solution of this issue is redundant vector duration time adjustment combined with space vector modulation theory [27]. Liu *et al.* [28] proposed a double-signal PWM technique that can control the NPP and reduce CMV simultaneously. However, the switching losses inside the inverter are increased. In [20], a series of virtual vectors are synthesized, and appropriate redundant vectors are selected based on the neutral point potential deviation. However, the number of candidate vectors is large, and the output is not stable enough. Yang *et al.* [29]–[31] added NPP error to the cost function as a constraint and solved the task of selecting the corresponding weighting factors for the multi-objective cost function. However, as mentioned above, weighting factor design in the cost function is complicated, especially when the number of control objectives increases.

Existing three-level FS-MPC methods usually design the cost function and traverse the candidate vectors to find the optimization. However, compared to the two-level inverter system, which has only 8 voltage vectors, there are 27 basic voltage vectors, even without considering the CMV and NPP imbalance features. Furthermore, in the $\alpha\beta$-plane, voltage vectors at the same position may correspond to different CMV amplitudes and multiple neutral point currents [32], [33]. To fill the abovementioned gap, this paper simplifies the process of voltage vectors selection and takes advantage of their CMV and NPP attributes. The main contributions of this work are as follows:

1) Since the three-level inverters provide abundant voltage vectors, regarding the computational burden of the system [17], an efficient mapping rule is introduced to narrow the candidate area into sub-hexagons. Numerical prediction and optimization stages are omitted, and a substantial amount of calculation time is saved. The vector operation time is determined by the cost function so as to minimize the tracking error.
2) The proposed scheme does not directly exclude the basic vectors with large CMV amplitudes [34], but rather reconstructs them into a set of vectors with equivalent outputs based on the current situation and regulation requirements. Then, in conjunction with the other vectors in the sub-hexagon at which they are located, the CMV suppression does not affect the other control effects in the vast majority of cases.
3) Without the need to model DC-bus capacitor charging and discharging, nor utilizing the opposite characteristics of the redundant vectors [22], a hysteresis controller is comprehensively designed based on the multiple characteristics of the space voltage vectors. It fully mobilizes various voltage vector resources and expands the bidirectional range to non-redundant vectors to collaboratively suppress NPP fluctuations and CMV.

The rest of this paper is organized as follows. Section II introduces the basic topology of 3L-NPC PMSM inverter drives and the principles of conventional FS-MPC. The novel position determination aimed at reducing the computational burden is put forward in Section III. Accordingly, RFS-MPC based on sub-hexagonal mapping is proposed. Section IV presents the multi-vector method with hysteresis control, which incorporates NPP balancing and CMV suppression into candidate set update and output vector recombination. The experimental studies of different MPC methods are given in Section V. In Section VI, the conclusions are drawn.

II. Model of 3L-NPC PMSM Drives and FS-MPC Methods

A. Topology and Switching States of 3L-NPC Inverter

Fig.1 shows the topology of the 3L-NPC inverter, V_{dc} is constant DC bus voltage, U_{C_1} and U_{C_2} are DC-link bus top and bottom capacitor voltages respectively. The two capacitors (C_1 and C_2) are charged to half of the DC bus voltage. Variables U_a, U_b and U_c respectively express the outputs of ABC three-phase arms.

Taking Phase A as an example, the four IGBTs, (S_{a1},S_{a3}) and (S_{a2},S_{a4}), are complementary switching pairs, with only

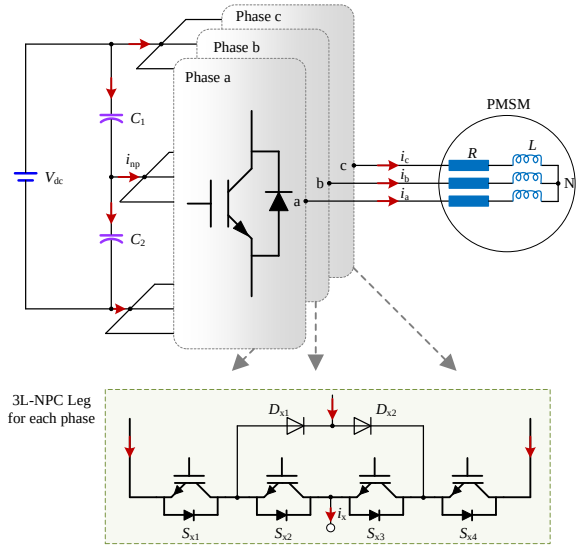

Fig. 1. Topology of three-level NPC inverter.

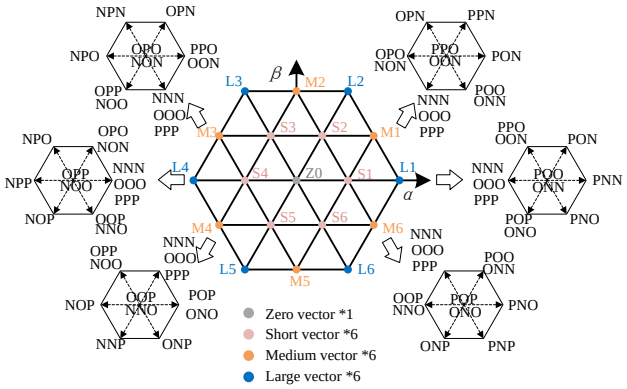

Fig. 2. Space voltage vectors diagram and 27 output states for the three-level inverter.

half the voltage stress on each IGBT compared to the two-level inverter. Each phase arm, therefore, has three switching states, the corresponding output value of U_a (U_b or U_c) may be $-\frac{V_{dc}}{2}$, 0 or $\frac{V_{dc}}{2}$. For convenience, $-\frac{V_{dc}}{2}$, 0 and $\frac{V_{dc}}{2}$ are labeled as N, O and P. Fig. 2 shows the total space voltage vectors diagram generated from 27 switching states.

B. Physical Model of PMSM and Control Methods

This paper focuses on surface-mounted PMSM, which have the same dq-axis stator inductances, i.e., L_d= L_q = L. The machine model in dq-axis can be expressed as follows:

$$\begin{cases} u_{ds} = R_s \cdot i_{ds} + L\frac{di_{ds}}{dt} - \omega_e \cdot L \cdot i_{qs} \\ u_{qs} = R_s \cdot i_{qs} + L\frac{di_{qs}}{dt} + \omega_e \left(L \cdot i_{ds} + \psi\right). \end{cases} \tag{1}$$

where i_{ds} and i_{qs} are the dq-axis components of the stator current; u_{ds} and u_{qs} are the d and q -axis stator voltages, respectively. R_s is the nominal stator resistance. ψ is the flux linkage generated by the permanent magnet on the rotor side;

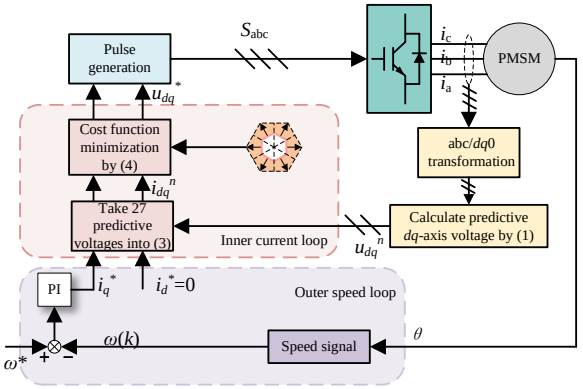

Fig. 3. Control diagram of the conventional FS-MPC.

ω_e is the rotor electrical speed. And the mechanical equations for a surface-mounted PMSM are shown as:

$$\begin{cases} T_e = \left(\frac{3p}{2}\right) \cdot \psi \cdot i_{qs} \\ T_e - T_l = J \cdot \frac{d\omega_e}{dt} + B_m \cdot \omega_e. \end{cases} \tag{2}$$

where, p is the number of pole pairs, J is the moment of inertia, T_e is the electromagnetic torque developed, T_l is the load torque, B_m is the viscous friction coefficient.

Then, the forward Euler algorithm is applied to (2), and discrete-time predictive dq-axis currents can be obtained, as shown in (3).

$$\begin{cases} i_d^{k+1} = i_d^k + \left(u_d^k - R_s i_d^k + pL\omega_r^k i_q^k\right) T_s/L \\ i_q^{k+1} = i_q^k + \left(u_q^k - R_s i_q^k - p\omega_r^k \left(L i_d^k + \psi\right)\right) T_s/L. \end{cases} \tag{3}$$

where T_s is the sampling time, k is the sampling interval. i_d^k, i_q^k and u_d^k, u_q^k are dq-axis stator currents and voltages in k-th instant, respectively. i_d^{k+1} and i_q^{k+1} are their predictions in $(k+1)$-th instant. ω_r^k is the rotor actual mechanical speed in k-th instant.

The conventional FS-MPC takes all 27 vectors into (3) to calculate predictive dq-axis currents at the next sampling time and then uses the predictive dq-axis currents to calculate cost function as follows:

$$g = \left|i_d^* - i_{d,i}^{k+1}\right| + \left|i_q^* - i_{q,i}^{k+1}\right|, i = 0, 1, \ldots, 26. \tag{4}$$

The vector that can minimize the cost function is selected and used in the next sampling time. The control diagram of the conventional FS-MPC control method with a 3L-NPC inverter is shown in Fig. 3, consisting of the outer speed loop and the inner stator current loop. Only one basic vector is selected per sampling cycle. Meanwhile, a total of 27 switching states are in the alternative list, and each basic vector needs to be predicted by (3) and calculated by (4), which causes a heavy computational burden on the processor and makes it difficult to operate at high switching frequency. The total calculation time per sampling period is up to 54, and 8 redundant voltage vectors are also accounted for.

III. Revised FS-MPC Method of Mapping to Sub-hexagons

The revised FS-MPC (RFS-MPC) is employed not only to reduce the computational burden but also to keep the

PMSM drive system running reliably. In the proposed RFS-MPC, the deadbeat MPC strategy is applied, in which the cost function of minimizing stator current tracking errors is converted to that of minimizing stator voltage tracking errors. The efficient position-determined method is introduced, in which the reference voltage vector is mapped to the sub-hexagon. Thus, the candidate area is narrowed and the number of calculations is significantly reduced.

A. Predictive Model Based on Deadbeat Principle

In terms of the principle of deadbeat control, the predictions of dq-axis stator currents in (k)-th instant can be assumed to reach their reference values. As a result, (3) can be modified as

$$\begin{cases} i_d^* = i_d^k + \left(u_d^k - R_s i_d^k + pL\omega_r^k i_q^k\right) T_s/L \\ i_q^* = i_q^k + \left(u_q^k - R_s i_q^k - p\omega_r^k \left(L i_d^k + \psi\right)\right) T_s/L. \end{cases} \tag{5}$$

According to the principle of maximum torque per ampere, i_d^* is set to zero. The dq-axis stator voltages u_d^k and u_q^k in (5) can be regarded as the desired references u_d^* and u_q^*, which can be deduced as

$$\begin{cases} u_d^* = R_s i_d^k - L\frac{i_d^k}{T_s} - L\omega_e^k i_q^k \\ u_q^* = R_s i_q^k + L\frac{i_q^* - i_q^k}{T_s} + L\omega_e^k i_d^k + \psi\omega_e^k. \end{cases} \tag{6}$$

where u_d^* and u_q^* are assumed to keep constant within every control cycle. Accordingly, the cost function can be defined for the RFS-MPC as

$$g_2 = \left|u_d^* - u_d^i\right| + \left|u_q^* - u_q^i\right|, i = 0, 1, 2, \ldots, 26. \tag{7}$$

From the above analysis, it can be seen that instead of multiple predictions in FS-MPC, the reference voltage is calculated only once in RFS-MPC during every control cycle. The execution time is reduced than that of the FS-MPC. Even so, a total of 27 elementary voltage vectors (including 8 redundant voltage vectors) need to be evaluated by (7), which is still causing a heavy calculation time. To further relieve the computational burden, it is effective to reduce the number of candidate elementary vectors, provided that the performance of the control system is not degraded. Through inverse Park transformation, the reference voltage vector is converted to the $\alpha\beta$ plane for sector judgment.

$$\begin{bmatrix} V_{\text{ref}}^\alpha \\ V_{\text{ref}}^\beta \end{bmatrix} = \begin{bmatrix} \cos\theta_e & -\sin\theta_e \\ \sin\theta_e & \cos\theta_e \end{bmatrix} \begin{bmatrix} u_d^* \\ u_q^* \end{bmatrix}$$
$$V_{\text{ref}} = V_{\text{ref}}^\alpha + jV_{\text{ref}}^\beta. \tag{8}$$

B. Sub-hexagon Mapping Rules in Three-Level Vector Space

To further simplify the localization and narrow the scope of the optimization search, the rule of mapping the three-level vectors into sub-hexagons is adopted. Unlike the traditional triangular subsector dividing approach [35], the one taken in this paper is the only one applicable to the subsequent scheme. As shown in Fig. 4, the original reference voltage vector V_{ref} in the stationary $\alpha\beta$-axis is mapped as $V_{\text{sub-ref}}$ in sub-hexagon I, which can be expressed as the difference between V_{ref} and the corresponding sub-hexagon center vector:

$$V_{\text{sub-ref}} = V_{\text{ref}} - u_{cv}. \tag{9}$$

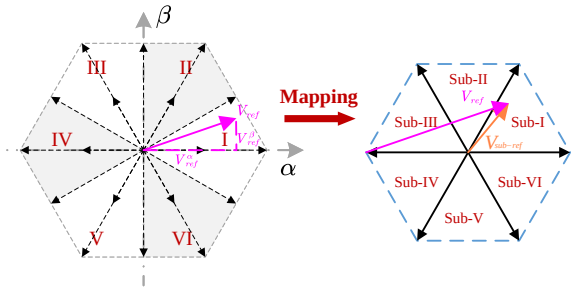

Fig. 4. Diagram of the original voltage vector and the mapping process.

TABLE I
CORRESPONDING RELATIONS BETWEEN SUB-HEXAGON AND INTERMEDIATE INDEXES

Sub-hexagon	I	II	III	IV	V	VI
X	1	1	0	0	0	1
Y	0	1	1	1	0	0
Z	0	0	0	1	1	1
N	1	3	2	6	4	5

where u_{cv} (cv = 1, 2, 3, 4, 5, 6) is the center vector according to the sector where the reference voltage vector lies.

Based on the length and angle of V_{ref}, it is possible to determine adjacent vectors directly. In order to facilitate the digital implementation of the algorithm, the following specific indicators are designed to determine geometric relationships based on a certain number of conditions. Here, the intermediate voltage variables V_X, V_Y, and V_Z are introduced, and their definitions are shown in (10). Define the intermediate indicator variables X, Y, Z and N according to the positive and negative values of the intermediate voltage variables, as shown in (11).

$$\begin{cases} V_{\text{X}} = V_{\text{ref}}^\alpha \\ V_{\text{Y}} = 3V_{\text{ref}}^\beta - \sqrt{3}V_{\text{ref}}^\alpha \\ V_{\text{Z}} = -3V_{\text{ref}}^\beta - \sqrt{3}V_{\text{ref}}^\alpha \end{cases} \tag{10}$$

$$X = \begin{cases} 1, & \text{if } V_{\text{X}} \geq 0 \\ 0, & \text{if } V_{\text{X}} < 0 \end{cases}$$
$$Y = \begin{cases} 1, & \text{if } V_{\text{Y}} \geq 0 \\ 0, & \text{if } V_{\text{Y}} < 0 \end{cases}$$
$$Z = \begin{cases} 1, & \text{if } V_{\text{Z}} \geq 0 \\ 0, & \text{if } V_{\text{Z}} < 0 \end{cases} \tag{11}$$
$$N = 4Z + 2Y + X.$$

Calculating the value of N uniquely determines the sector where V_{ref} is locate. Taking sub-hexagon I as an example, $V_{\text{X}} \geq 0$, $V_{\text{Y}} < 0$, $V_{\text{Z}} < 0$, and thus $X = 1$, $Y = 0$, $Z = 0$, $N = 1$. The corresponding relationship between the sub-hexagon number and the values of the intermediate indicator variables X, Y, Z, and N is shown in Table I.

TABLE II
CORRESPONDING RELATIONS BETWEEN SMALL SECTORS AND INTERMEDIATE INDEXES

Small sector	I	II	III	IV	V	VI
X_{sub}	1	1	1	0	0	0
Y_{sub}	1	0	0	0	1	1
Z_{sub}	0	0	1	1	1	0
M	3	1	5	4	6	2

To further pinpoint the positioning, continue sectoring in the sub-hexagons. The small sector number where $V_{\text{sub-ref}}$ is located can be determined as follows:

$$\begin{cases} V_{\text{X-sub}} = V^{\beta}_{\text{sub-ref}} \\ V_{\text{Y-sub}} = 3V^{\alpha}_{\text{sub-ref}} - \sqrt{3}V^{\beta}_{\text{sub-ref}} \\ V_{\text{Z-sub}} = -3V^{\alpha}_{\text{sub-ref}} - \sqrt{3}V^{\beta}_{\text{sub-ref}} \end{cases} \tag{12}$$

$$\begin{aligned} X_{\text{sub}} &= \begin{cases} 1, & \text{if } V_{\text{X-sub}} > 0 \\ 0, & \text{if } V_{\text{X-sub}} \le 0 \end{cases} \\ Y_{\text{sub}} &= \begin{cases} 1, & \text{if } V_{\text{Y-sub}} > 0 \\ 0, & \text{if } V_{\text{Y-sub}} \le 0 \end{cases} \\ Z_{\text{sub}} &= \begin{cases} 1, & \text{if } V_{\text{Z-sub}} > 0 \\ 0, & \text{if } V_{\text{Z-sub}} \le 0 \end{cases} \\ M &= 4Z_{\text{sub}} + 2Y_{\text{sub}} + X_{\text{sub}}. \end{aligned} \tag{13}$$

Similarly, the correspondence of M is shown in Table II. After the above series of processes, the reference voltage vector is accurately positioned in a small sector of the sub-hexagon. At this time, the number of predictions has been greatly reduced, and only three adjacent vectors in the small sector need to be evaluated, and the optimal candidate vector among them is determined based on the nearest distance principle. This approach redefines the cost function and avoids the tedious process of repeated predictions.

IV. PROPOSED MULTI-VECTOR MPC WITH CMV SUPPRESSION AND NPP BALANCE

A. Analysis of CMV Generation and NPP Imbalance

As illustrated in Fig. 2, we can observe that for a 3L-NPC inverter, a total number of 27 switching states are available. Out of which, 6 are large voltage vectors (LVV) of the amplitude. When these vectors are applied, the three phases are either connected to the positive or negative rail and the loads are not connected to the neutral point. Therefore, LVVs do not cause a change in the neutral point voltage. For the 3 zero voltage vectors (ZVV), all three phase loads are short-circuited to the same rail and thus do not affect the NPP either. For the 6 medium (MVV) and 12 small vectors (SVV), at least one of the three phases is connected to the neutral point of the capacitor and forms a current with the positive and negative rail of the DC supply.

When the MVV or the SVV are applied, the upper capacitor C_1 and the lower capacitor C_2 are charged and discharged by the current I_{np}, thus causing the NPP drift. Each pair of

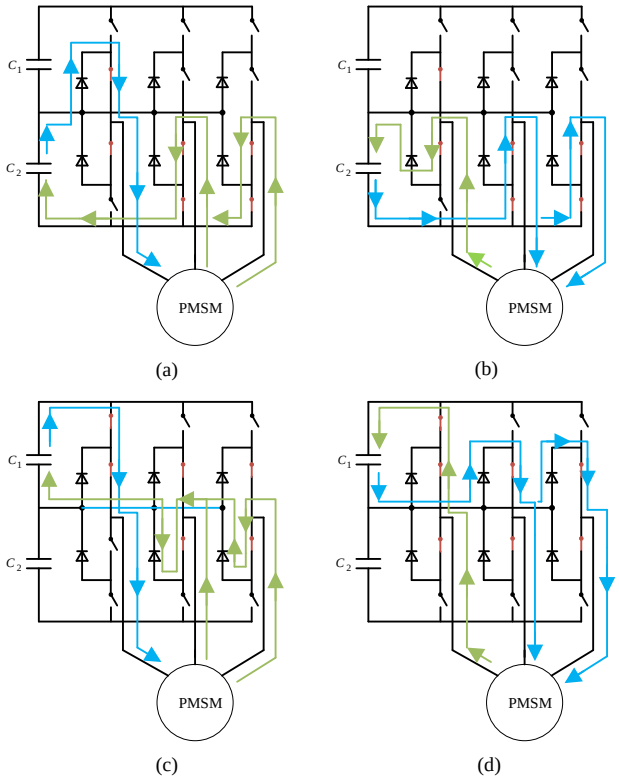

Fig. 5. SVVs operating states and their corresponding neutral point currents. (a)V_4(ONN),$i_a > 0$ (b)V_4(ONN),$i_a < 0$ (c)V_3(POO),$i_a > 0$ (d)V_3(POO),$i_a < 0$.

redundant SVVs has the opposite polarity of the I_{np} although the output voltage state is the same, so they can be used to mitigate the NPP drift caused by the MVVs. All the 27 switching states and different types of voltage vectors can be found in Table III. Fig. 5 takes the switching states of V_3 and V_4 as an example to explain the relationship between the neutral point current and the phase currents. Fig. 2 shows that the positions of V_4 and V_3 are the same, but the effect on NPP is just opposite. Define SVV connected to the positive end of the DC bus like V_4 as a positive small voltage vector (SVV (+)), and SVV connected to the negative end of the DC bus like V_3 as a negative small voltage vector (SVV (-)).

The CMV is essentially the zero-sequence component widely present in inverters and is defined as the potential difference between the load neutral and the reference ground.

$$\begin{aligned} V_{AO} &= V_{AN} + V_{NO} \\ V_{BO} &= V_{BN} + V_{NO} \\ V_{CO} &= V_{CN} + V_{NO} \end{aligned} \tag{14}$$

where, V_{AN}, $V_{BN}$and V_{CN} are the three phases voltages, and V_{AO}, V_{BO} and V_{CO} are the pole voltages. V_{NO} is the voltage difference between the neutral point of the PMSM and the neutral point of the capacitors. As for a balanced three-phase system, the sum of the three-phase voltages is zero. Thus, the definition of V_{CMV} is

$$V_{CMV} = \frac{V_{AO} + V_{BO} + V_{CO}}{3} \tag{15}$$

TABLE III
SWITCHING STATES AND ITS CORRESPONDING NEUTRAL CURRENT

Vector categories	Voltage level	Switching state and neutral current		
ZVV	0 (Null)	V_0(NNN)	V_1(OOO)	V_2(PPP)
		0	0	0
SVV	$V_{dc}/3$	V_3(POO)	V_7(OPO)	V_6(OON)
		$-I_a$	$-I_b$	$-I_c$
		V_4(ONN)	V_8(NON)	V_5(PPO)
		I_a	I_b	I_c
		V_{10}(NOO)	V_{14}(ONO)	V_{11}(OOP)
		$-I_a$	$-I_b$	$-I_c$
		V_9(OPP)	V_{13}(POP)	V_{12}(NNO)
		I_a	I_b	I_c
MVV	$V_{dc}/\sqrt{3}$	V_{18}(OPN)	V_{16}(PON)	V_{20}(NPO)
		I_a	I_b	I_c
		V_{24}(ONP)	V_{22}(NOP)	V_{26}(PNO)
		I_a	I_b	I_c
LVV	$2V_{dc}/3$	V_{15}(PNN)	V_{17}(PPN)	V_{19}(NPN)
		0	0	0
		V_{21}(NPP)	V_{23}(NNP)	V_{25}(PNP)
		0	0	0

According to (15), the CMVs for the 27 voltage vectors are listed in Table IV. It is shown that MVVs and V_1(OOO) produce zero CMV, and if space vectors with larger CMVs are aborted, CMV can be controlled within $\pm V_{dc}/3$.

B. RFS-MPC Integrating with CMV Suppression

From the above analysis, it can be seen that the basic zero voltage vector is generally used OOO switch state. The magnitude of its CMV is zero, whereas the CMVs generated by the switch state PPP and NNN are large, so they will not be used in the proposed method. MVVs have no effect on the CMV, while the SVVs(+) cause the system to generate a large CMV during operation. And the CMV generated by SVV(-) is only half of the CMV generated by SVVs(+), so the use of SVVs(+) should be avoided in constructing the alternative vectors.

In order to improve the SVV(+), it is considered to be composed of a fundamental zero vector OOO and a fundamental LVV. This method can solve the problem of large CMV in a more ideal way. When the SVV(+) is not excluded, the CMV can be as large as $\pm V_{dc}/3$. In the improved scheme, the CMV amplitude is reduced to $\pm V_{dc}/6$, which is only half of the original one.

$$\begin{cases} \boldsymbol{V}'_{\mathrm{s1}} = \frac{1}{2}\boldsymbol{V}_{0(\mathrm{OOO})} + \frac{1}{2}\boldsymbol{V}_{\mathrm{L1(PNN)}} \\ \boldsymbol{V}'_{\mathrm{s2}} = \frac{1}{2}\boldsymbol{V}_{0(\mathrm{OOO})} + \frac{1}{2}\boldsymbol{V}_{\mathrm{L2(PPN)}} \end{cases} \tag{16}$$

At this point, in conjunction with the RFS-MPC mapping approach in Section II, the transformed SVV is used as the center point of each sub-hexagon. This also paves the way for the multi-vector MPC algorithm that follows.

C. NPP Hysteresis Balance Based on Multipolarity of Space Vectors

In the previous subsection, the synthesis of SVV was accomplished using ZVV and LVVs. In contrast to the use of SVV(-) in place of SVV(+), the proposed scheme does not produce a neutral point current in the synthesized SVVs because the ZVV and LVVs do not produce a current at the neutral point. However, in order to achieve a purposeful regulation of the NPP, it is necessary to recombine a set of fundamental vectors that act opposite to the NPP and to design a controller that does not need to take into account the system parameters. The whole control diagram is illustrated in Fig. 6.

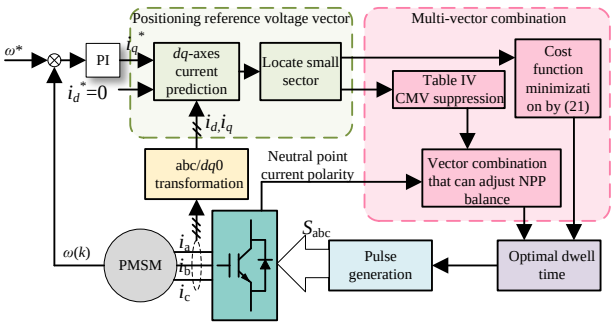

Fig. 6. Control diagram of the proposed method.

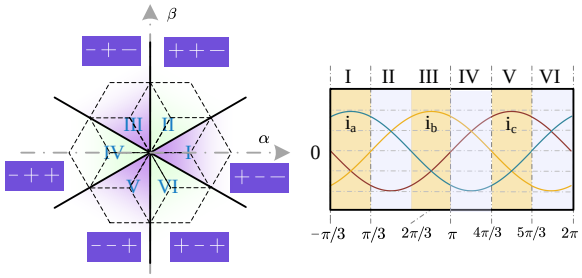

Fig. 7. Direction of Three-phase Current in the Voltage Vector Figure.

1) Principle of the Proposed Multi-Vector Strategy: When the 3L-NPC inverter drives the PMSM, the three-phase bridge arm output voltage is related to the direction of the load current. Fig. 7 shows the position of the voltage space vector and the direction of the three-phase current at this time. Taking the angle of V_{ref} as 15^o, mapped to the sub-hexagon I. The directions of the ABC three-phase currents are $+--$.

In the previous subsection, we analyzed the effects of various voltage vectors on the NPP balance. Taking the MVV V_{16}(PON) as an example, during its dwell time T_m, the charge q_{T_m} flowing out of the neutral point O of the voltage dividing capacitors due to the three-phase load current is:

$$q_{T_{\mathrm{m}}} = \int_0^{T_{\mathrm{m}}} I_{\mathrm{a}}\mathrm{d}t + \int_0^{T_{\mathrm{m}}} I_{\mathrm{b}}\mathrm{d}t + \int_0^{T_{\mathrm{m}}} I_{\mathrm{c}}\mathrm{d}t. \tag{17}$$

If $I_b < 0$ and the charge flowing out of neutral point O $q_{T_m} < 0$, then U_{C_1} becomes smaller and U_{C_2} becomes larger; if $I_b > 0$ and the charge flowing out of neutral point O $q_{T_m} > 0$, then U_{C_1} becomes larger and U_{C_2} becomes smaller. And since, as mentioned earlier, the current I_b is always negative throughout the sub-hexagon I, the influence exerted by the original MVV on the NPP balance is also in a fixed direction.

TABLE IV
SPACE VECTORS AND CORRESPONDING CMV

LVV	V_{CMV}	MVV	V_{CMV}	SVV(+)	V_{CMV}	SVV(-)	V_{CMV}	ZVV	V_{CMV}
V_{15}	$-V_{dc}/6$	V_{16}	0	V_4	$-V_{dc}/3$	V_3	$V_{dc}/6$	V_0	$-V_{dc}/2$
V_{17}	$V_{dc}/6$	V_{18}	0	V_5	$V_{dc}/3$	V_6	$-V_{dc}/6$	V_1	0
V_{19}	$-V_{dc}/6$	V_{20}	0	V_8	$-V_{dc}/3$	V_7	$V_{dc}/6$	V_2	$V_{dc}/2$
V_{21}	$V_{dc}/6$	V_{22}	0	V_9	$V_{dc}/3$	V_{10}	$-V_{dc}/6$		
V_{23}	$-V_{dc}/6$	V_{24}	0	V_{12}	$-V_{dc}/3$	V_{11}	$V_{dc}/6$		
V_{25}	$V_{dc}/6$	V_{26}	0	V_{13}	$V_{dc}/3$	V_{14}	$-V_{dc}/6$		

2) Multi-Vector Dwell Time Calculation: In the conventional multi-vector MPC method, dwell times for two adjacent voltage vectors and the zero vector are calculated from a geometric relationship. In this paper, we refer to the method in [5], optimizing the switching time by the cost function. Assuming that the mapping reference voltage vector falls in the first small sector of sub-hexagon I, analyze the vector selection case and the dwell times. At this time, the original vectors closest to the reference voltage are V_3/V_4, V_{15} and V_{16}. First, based on the amplitude-second balance principle of the space vector, the following equation can be obtained:

$$\begin{cases} V_{\mathrm{e}0}T_0 + V_{\mathrm{e}1}T_1 + V_{\mathrm{e}2}T_2 = V_{\mathrm{ref}}T_{\mathrm{s}} \\ T_0 + T_1 + T_2 = T_{\mathrm{s}} \end{cases} \tag{18}$$

where $V_{\mathrm{e}0}$ is the equivalent vector of the MVV V_{16} and T_1 is its dwell time. $V_{\mathrm{e}1}$ is the equivalent vector of the LVV V_{15} and T_2 is its dwell time. $V_{\mathrm{e}2}$ is the equivalent vector of the SVV V_3/V_4 and T_0 is its dwell time.

The reference voltage vector can be regarded as constant over a cycle. Therefore, transform (18) into the $\alpha\beta$ coordinate system:

$$\begin{cases} T_s V_\alpha = V_{\alpha1}T_1 + V_{\alpha2}T_2 + V_{\alpha0}T_0 \\ T_s V_\beta = V_{\beta1}T_1 + V_{\beta2}T_2 + V_{\beta0}T_0 \\ T_0 + T_1 + T_2 = T_{\mathrm{s}} \end{cases} \tag{19}$$

where $V_{\alpha1}$, $V_{\alpha2}$ and $V_{\alpha0}$ are the α-axis component of the three selected voltage vectors. $V_{\beta1}$, $V_{\beta2}$ and $V_{\beta0}$ are the β-axis component. The duration ratio of the symmetrical vectors d_1, d_2 and d_0 can be obtained by normalizing dwell times T_1, T_2 and T_0, respectively.

$$\begin{cases} V_\alpha = V_{\alpha1}d_1 + V_{\alpha2}d_2 + V_{\alpha0}d_0 \\ V_\beta = V_{\beta1}d_1 + V_{\beta2}d_2 + V_{\beta0}d_0 \\ d_0 = T_0/T_s \\ d_1 = T_1/T_s \\ d_2 = T_2/T_s. \end{cases} \tag{20}$$

In Section II, the predictive voltage is adopted as the desired value u_d^* in the next sampling time. The cost function can be defined as follows to obtain the optimal solution of d_1, d_2 and d_0.

$$g = \left(u_\alpha^* - V_\alpha\right)^2 + \left(u_\beta^* - V_\beta\right)^2. \tag{21}$$

where u_α^* and u_β^* are the predictive voltages. Taking partial derivatives of (21) yields

$$\begin{cases} \frac{\partial g}{\partial d_1} = \frac{\partial\left((u_\alpha^* - V_\alpha)^2 + \left(u_\beta^* - V_\beta\right)^2\right)}{\partial d_1} = 0 \\ \frac{\partial g}{\partial d_2} = \frac{\partial\left((u_\alpha^* - V_\alpha)^2 + \left(u_\beta^* - V_\beta\right)^2\right)}{\partial d_2} = 0. \end{cases} \tag{22}$$

Calculating (20) and (22) gives d_1 and d_2 as

$$\begin{cases} d_1 = (AC - BD)/\left(B^2 - A^2\right) \\ d_2 = (AD - BC)/\left(B^2 - A^2\right) \end{cases} \tag{23}$$

where

$$\begin{cases} A = V_{\alpha1}^2 + V_{\beta1}^2 \\ B = V_{\alpha1}V_{\alpha2} + V_{\beta1}V_{\beta2} \\ C = -u_\alpha^* V_{\alpha1} - u_\beta^* V_{\beta1} \\ D = -u_\alpha^* V_{\alpha2} - u_\beta^* V_{\beta2}. \end{cases} \tag{24}$$

The novel method is called optimal dwell time MPC. Its computational complexity is greatly reduced. On the basis of one-time prediction deadbeat control, the output error is further reduced, and the control accuracy is improved. After the center vector of the corresponding sub-hexagon is found out, the three resultant voltage vectors in the mapping sector are applied and switched in the optimal moments.

3) NPP Hysteresis Balance Controller Design: Based on the previous analysis in subsection A, the NPP polarity of the final output voltage is dependent on the NPP polarities of the SVV and MVV selected in this control cycle. Therefore, the neutral point current can be effectively controlled by adjusting the combination of voltage vectors. According to this sampling period's detected neutral point current polarity, the SVV and MVV opposite to the current polarity is output. The principle of hysteresis control is shown in Fig. 8. However, the MVVs have no redundancy and can only balance the NPP from a fixed polarity, whereas the SVVs, despite being paired, where SVV(+) need to be avoided due to higher CMV.

In each sampling period, one equivalence short voltage vector and two voltage vectors on the boundary of small sectors are employed. This part will use this switch states recombination feature to achieve NPP hysteresis control. Defining the voltage vectors at the six sub-hexagons centers as V'_{si}. According to the multi-vector MPC method proposed in this paper, the output synthesized vector can only appear in the following three cases. Taking the sub-hexagon centered at V_3/V_4 as an example (as shown in Fig. 5), the switch states selection principle is explained as follows.

Case 1: the candidate voltage vectors are two SVVs and one ZVV in terms of magnitude. Because the SVV(+) is replaced

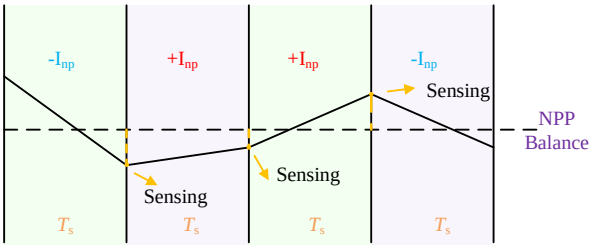

Fig. 8. Scheme of NPP Balance hysteresis control.

by a combined vector of LVV and ZVV, given its larger CMV, NPP hysteresis control can be achieved just by selecting one proper SVV(-) and one V'_{si}. If $U_{C_1} > U_{C_2}$, the SVV(-) with negative q_{T_m} are selected as the output. In sub-hexagon I, $I_a > 0$, $I_b < 0$, $I_c < 0$, thus V_3(POO) is the proper switch state. If $U_{C_1} < U_{C_2}$, the SVV(-) with positive q_{T_m} are selected as the output. Thus V_6(OON)/V_{14}(ONO) is the proper switch state. For the other two vectors, ZVV V_1(OOO) and the corresponding position of V'_{si} are chosen. None of them will cause NPP fluctuations, and the CMV is also very small.

Case 2: the candidate voltage vectors are two SVVs and one MVV in terms of magnitude. In sub-hexagon I, the two MVVs V_{16}(PON)/V_{26}(PNO) produce neutral currents I_b and I_c, which are all negative polarity. If $U_{C_1} > U_{C_2}$, the SVV(-) with negative q_{T_m} are selected as the output. Thus V_{16}(PON)/V_{26}(PNO) is the proper switch state. If $U_{C_1} < U_{C_2}$, the overall output need to be of positive q_{T_m}. This can be achieved by rationally utilizing the MVVs and SVVs. According to Fig. 7, within the second small sector of the sub-hexagon I, the absolute value of I_c is always less than I_b. Therefore, the total polarity of V_6 and V_{16} is positive and still applies to the case where $U_{c_1} < U_{c_2}$. By the above method, although the neutral point current of MVV is not adjustable, reliable suppression of the NPP unbalance can still be ensured.

Case 3: the candidate voltage vectors are one SVV, one MVV and one LVV in terms of magnitude. In this case, the candidate space vectors have the same negative polarity neutral point current. When $U_{C_1} > U_{C_2}$, hysteresis control can be achieved by outputting them. But when $U_{C_1} < U_{C_2}$, even if the equivalent combinations of the SVV is V'_{s1} with no neutral point current, the NPP polarity of the output vector is still negative and the hysteresis control fails. To cope with this situation, take the center vector replacement method. When $U_{C_1} < U_{C_2}$, replacing the center vector with a positive polarity neutral point current corrects the NPP of the resultant voltage vector to zero. Although the CMV amplitude of SVV(+) is larger, it is temporarily used to achieve NPP balance. When the reference voltage vector is located in other sub-hexagons, the switching state of the center vector that needs to be replaced also changes, but in principle, such measures can always have a negative feedback effect.

All voltage vectors and neutral current polarities in sub-hexagon I are labeled as shown in Fig. 9, with black indicating 0, green indicating positive, and red indicating negative. The mechanisms of the above three cases are summarized in Table

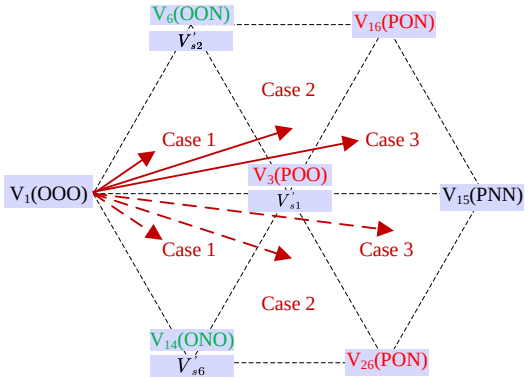

Fig. 9. Scheme of vectors combination selection.

TABLE V
SUMMARY OF NPP HYSTERESIS CONTROL

Nearest three-vector combination type	NPP polarity	Small sector number	Selected voltage vectors	Center vector replace
Case 1	$U_{C_1} > U_{C_2}$	3	V_3, V_1, V'_{s2}	No need
		4	V_3, V_1, V'_{s6}	No need
	$U_{C_1} < U_{C_2}$	3	V'_{s1}, V_1, V_6	No need
		4	V'_{s1}, V_1, V_{14}	No need
Case 2	$U_{C_1} > U_{C_2}$	2	V_3, V'_{s2}, V_{16}	No need
		5	V_3, V'_{s6}, V_{26}	No need
	$U_{C_1} < U_{C_2}$	2	V'_{s1}, V'_{s2}, V_{16}	No need
		5	V'_{s1}, V'_{s6}, V_{26}	No need
Case 3	$U_{C_1} > U_{C_2}$	1	V_3, V_{15}, V_{16}	No need
		6	V_3, V_{15}, V_{26}	No need
	$U_{C_1} < U_{C_2}$	1	V_4, V_{15}, V_{16}	Need
		6	V_4, V_{15}, V_{26}	Need

V. $U_{C_1} < U_{C_2}$ in Case 3 needs to replace center vector, which has a certain impact on the current control performance. Apart from this, in other cases, it only changes the switch state and does not affect the position of the output voltage vector. This hysteresis control method provides a more robust suppression of NPP imbalance without the need to model the neutral point current. In addition, the regulation process is simple without the need to fine-tune the weighting factors or recalculate the action time of the active vector. By simulating the execution time of each process in the algorithm, it can be found that the computation time of the proposed strategy is only 19.6 μs, of which CMV suppression and NPP balancing account for only 24.4% of the computation amount.

D. Overall Control Scheme

Fig. 10 illustrates the flowchart for the proposed method, which begins with the calculation of dq-axis predictive voltages of PMSM. Then they are transformed to $\alpha\beta$-axis, and the sub-hexagon can be located. The mapping $\alpha\beta$-axis predictive voltages are used to obtain two adjacent voltage vectors and center voltage vectors. The optimal dwell times of multi-vector are calculated using the cost function. The computational burden is greatly reduced and the reference voltage is generated more accurately.

In order to achieve CMV suppression and NPP balance, a hysteresis controller is designed. After the selection of the candidate voltage vectors is completed and the dwell time is

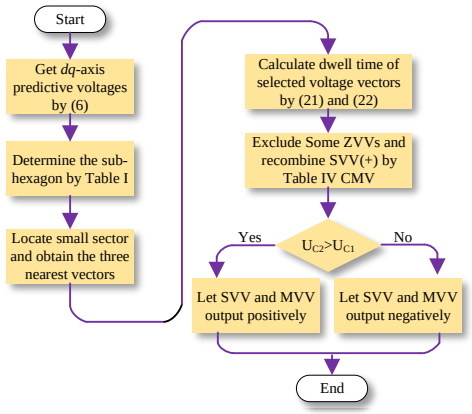

Fig. 10. Flowchart of the proposed scheme.

TABLE VI
PMSM AND CONTROLLER PARAMETERS

Parameters	Value	Unit	Parameters	Value	Unit
Stator Resistance (R_s)	0.65	Ω	Flux Linkage (ψ_m)	0.225	Wb
d-axis Inductance (L_d)	1.55e-3	H	q-axis Inductance (L_q)	1.55e-3	H
Rated Speed (n)	1000	r/min	Deadtime (t_d)	2.5	μs
Torque Constant (K_t)	0.552	N · m/A	Inertia (J)	8.58e-4	kg · m^2
DC-link capacitors (C_1)	902	μF	Rated Torque	6	N · m
Machine Pole Pairs (p)	4		Encoder Resolution	5000	PPR

determined, according to the detected polarity of the neutral point current in this sampling cycle, the vectors combination is adjusted. Finally, the 3L-NPC inverter outputs NPP opposite to the polarity of the neutral point current. Compared to the existing strategies, the proposed strategy is easily implemented and gets rid of the dependence on the motor model.

V. Experimental Results Verification

A. PMSM Test Rig Setup

To validate the feasibility of the proposed low computational burden MPC with NPP balance and CMV suppression, the hardware experimental results are obtained on a PMSM platform. The photograph of the experimental test rig is shown in Fig. 11. The oscilloscope is the high performance Tektronix MDO4024HD. Under different working conditions of the experiment, the switching frequency is in the range of 4-8khz, which is suitable for practical application scenarios of high voltage and high power. A high-power DC supply powers the three-level NPC inverter, and an independent small power supply powers the encoder of the PMSM. The loading is provided with the help of a magnetic powder brake and an external tension controller. The MicroLabBox dSPACE 1202 is chosen as the main controller. The PMSM and controller parameters are listed in Table VI.

B. Steady-State Performance and Dynamic Response Comparison

The performance of the proposed schemes is evaluated by conducting comprehensive comparisons with RFS-MPC and conventional multi-vector MPC (CMV-MPC) proposed in [18]. First, the steady-state performance of the three approaches is

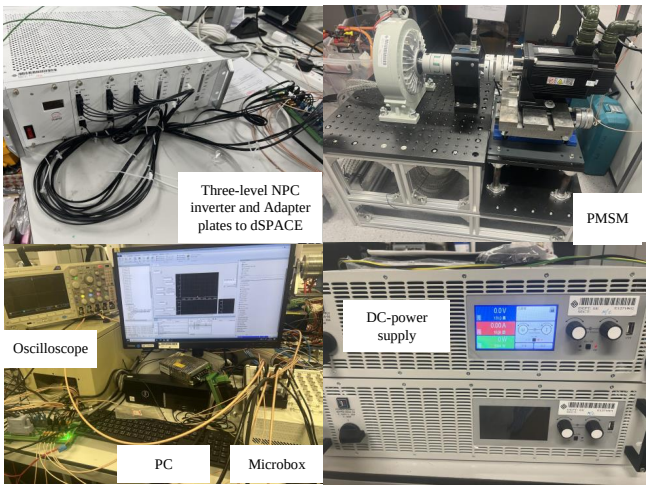

Fig. 11. PMSM test rig setup.

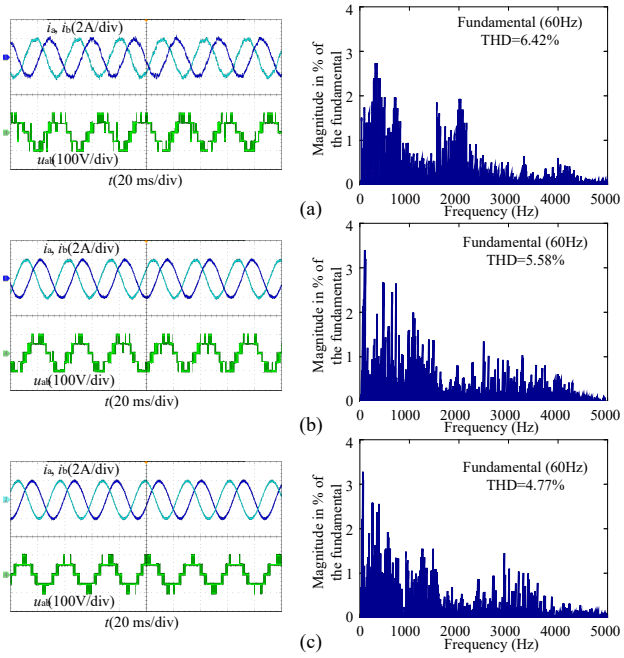

Fig. 12. Steady-state performance comparison at 500 r/min and 3Nm load. (a) RFS-MPC. (b) CMV-MPC. (c) Proposed method.

tested under 500 r/min (50% rated speed) with a load of 3 N·m. The line-line voltage and the phase currents corresponding to different methods are shown in 12, respectively. The comparative experiment was also carried out under the operation mode of rated speed and load, and the results are shown in 13. From the current spectrum, it can be observed that the proposed method has the lowest current distortion among the three approaches under different operating modes as it further optimizes the dwell times.

The THD of RFS-MPC is significantly greater than that of CMV-MPC and the proposed method. This is because RFS-MPC selects the output voltage vector according to the region where the calculated reference voltage is located and maintains a single output throughout the control cycle. As shown in Fig.

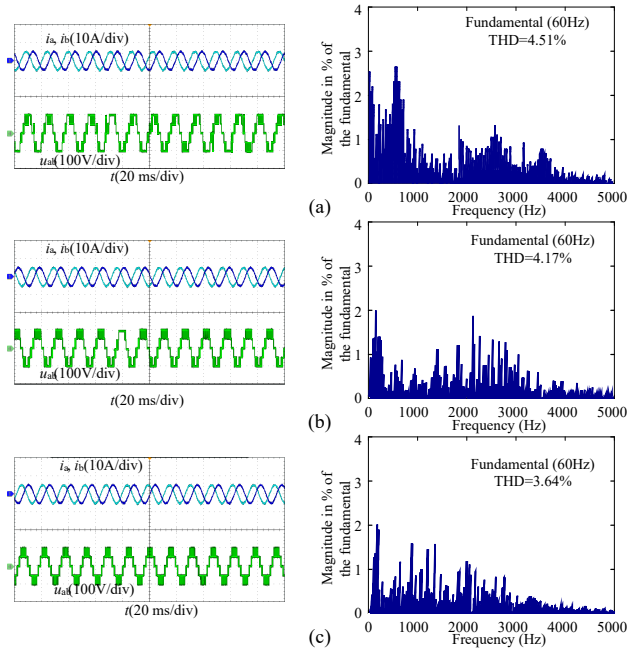

Fig. 13. Steady-state performance comparison at rated speed and load. (a) RFS-MPC. (b) CMV-MPC. (c) Proposed method.

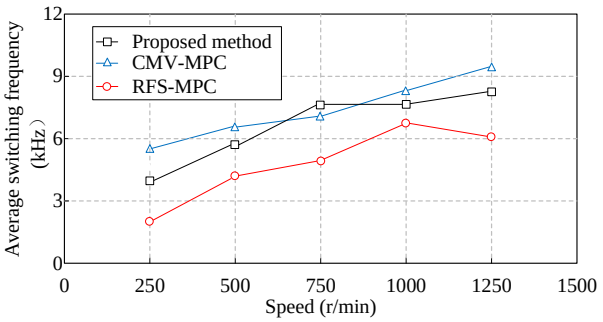

Fig. 14. Average switching frequencies comparison under different speeds.

14, the average switching frequency of RFS-MPC will always be lower than that of the other two methods if operated at the same sampling frequency. This is true over the entire speed range, especially when the motor is running at low speeds, where zero vector is selected most of the time.

The power test verifies that the inverter loss of the proposed scheme is lower than that of CMV-MPC under different operating conditions. Despite the NPP balance, CMV suppression, and excellent control effect, it does not actuate the switching device more frequently. The switching devices of the 3L-NPC inverter system are 1.5 times that of the two-level system. Thus, the switching loss is more significant. It makes excellent sense to reduce the switching frequency as much as possible, like the proposed method.

It is also essential to analyze the transient behavior of the PMSM drive and ascertain the dynamic response capability of the proposed approach with the rated load. Fig. 15(a) shows the q-axis current and speed response to a sudden change in reference speed from 400 r/min to 750 r/min. It can be

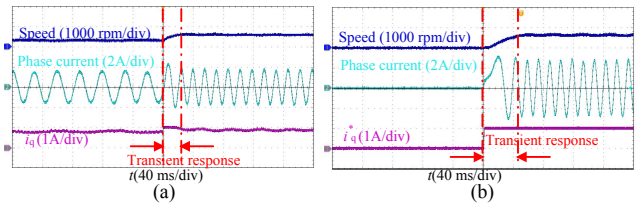

Fig. 15. Dynamic response of the proposed method. (a) Speed change from 400 r/min to 750 r/min. (b) Motor starts to rated speed.

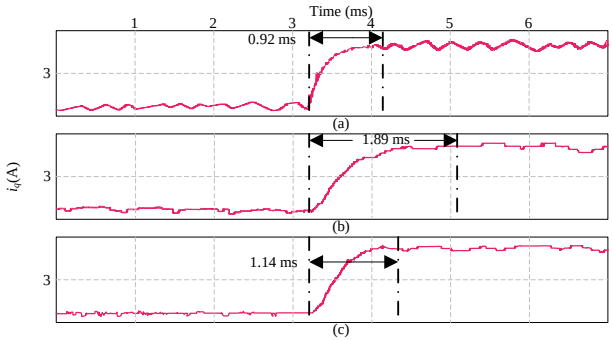

Fig. 16. Comparison of transient performance when the speed loop is removed, and the q-axis reference current is given as 4A. (a) RFS-MPC. (b) CMV-MPC. (c) Proposed method.

seen that the proposed strategy can make a quick response to complete the acceleration process. Moreover, Fig. 15(b) shows the drive response when the motor starts to rate speed. Fig. 16 shows the transient performance comparison of different methods when the q-axis reference current is set to 4A. The settling time of CMV-MPC is the longest, while the proposed method took 1.14 ms to track the reference current, slightly slower than RFS-MPC. These results demonstrate that the proposed method has satisfactory dynamic performance. During the full speed range, the major contribution of the proposed method is to relieve the computational burden at a similar switching frequency range, besides certain improvements in motor performance.

C. NPP Balance and CMV Suppression Test

Two tests were conducted to verify the NPP balancing effect of the proposed method. First, the capacitors voltages before and after the proposed scheme is put into use are compared, and the experimental results are shown in Fig. 17(a). It can be observed that the imbalance is serious at the beginning, and the voltage difference between the upper capacitor and the lower capacitor U_{C_1}-U_{C_2} on the DC side is about 15V. After the proposed method is put into use, two capacitor voltages tend to be same and their fluctuations are restricted within the range of [-5, 5] most of the time. The proposed method achieves significant results for the control of NPP. The dynamic response of the NPP balance effect is shown in Fig. 17(b) when the motor speed is changed from 500 r/min to 1000 r/min, and the capacitors voltage difference remains stable. The comparison experiment with CMV-MPC is presented in Fig. 18, which indicates that the proposed method has a better NPP balancing capability in the full speed range.

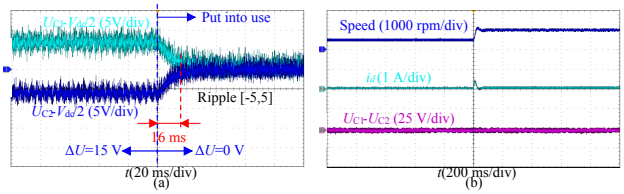

Fig. 17. Two tests of NPP balance. (a) Comparison before and after application of the proposed method. (b) NPP suppression effect dynamic response.

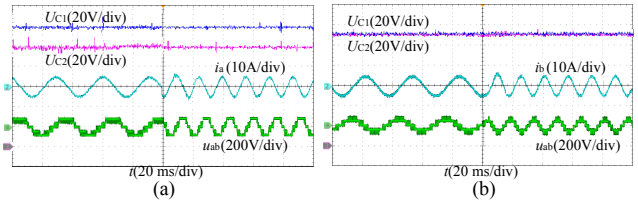

Fig. 18. Response of speed change from 500 to 1000 r/min with rated load for (a) CMV-MPC. and (b) proposed method.

On the other hand, the CMV suppression effect of the proposed method is shown in Fig. 19. Due to the application of V_0(NNN), V_2(PPP), and SVVs(+), the amplitude of CMV is up to $\pm V_{dc}/2$ before the proposed algorithm is put into use. It should be noted that the magnitude of CMV is reduced to less than 50 V immediately when the proposed strategy is applied. The dynamic effectiveness of CMV suppression is proved while, at the same time, the capacitors voltages can be properly balanced to $V_{dc}/2$. Fig. 20 shows the experimental waveforms at high modulation indices. The THD of CMV-MPC is 5.39%, while the proposed scheme has higher current quality, but its CMV suppression effect is somewhat reduced, because Case 3 requires the use of SVV(+).

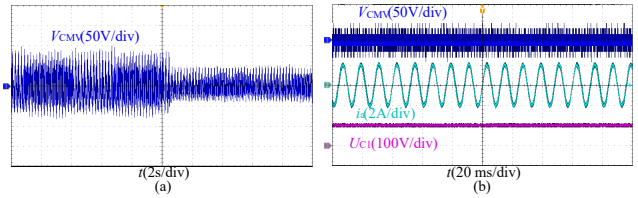

Fig. 19. CMV suppression effect. (a) Dynamic waveforms of CMV. (b) Integrated situation under stable operation.

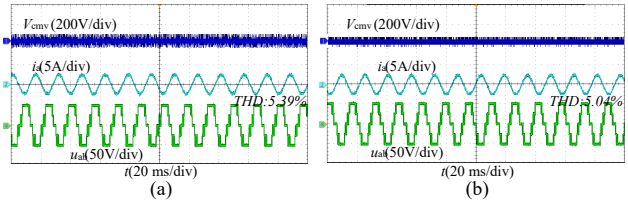

Fig. 20. Experimental waveforms of the different methods at a modulation index of 1. (a) CMV-MPC. (b) the proposed method.

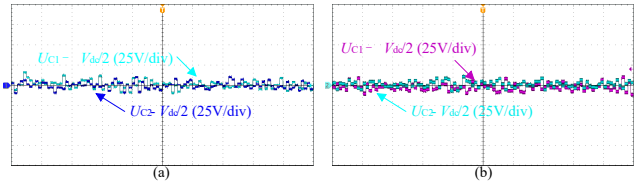

Fig. 21. NPP unbalance suppression effect of the proposed algorithm. (a) Accurate capacitance parameters. (b) Capacitor increased to 150% of actual value.

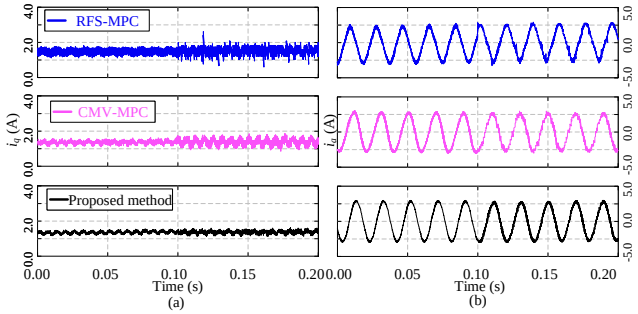

Fig. 22. Robustness against resistance parameter mismatch comparison of three methods. (a) q-axis currents. (b) A-phase stator current.

D. Robustness Against Parameters Mismatch Test

The hysteresis control adopted by the proposed method is independent of the capacitor model parameters. A comparative experimental study is carried out to verify the effectiveness of the proposed method in balancing NPP when the capacitor parameters are inaccurate. Fig. 21 illustrates that the effect of balancing U_{C_1} and U_{C_2} of the proposed method is not influenced by the capacitor parameter mismatch. In terms of motor parameters, it mainly involves resistance, inductance and flux linkage, and their maximum range of variation is also determined experimentally. Fig. 22 shows the comparative results of RFS-MPC, CMV-MPC, and the proposed method for stator resistance mismatch. The motor operates at 800 rpm with rated load, and at 0.10 s, the model resistance suddenly changes to 150% of the actual value. The phase current fluctuation and the q-axis ripple based on the proposed method are the lowest. The steady state current performance with mismatched inductance and flux parameters is shown in Fig. 23. Despite the slight increase in THD, the waveforms are stable and sinusoidal. The proposed method has some sensitivity to the motor parameters, especially the inductance, but still operates stably at 0.5 times mismatch.

E. Algorithm Execution Time Test

To verify the computational efficiency of the proposed methods, the turnaround time was read directly in the dSPACE1202 control system. Fig. 24 shows the algorithm execution time for different scenarios under the same control period of 50μs. For a fair comparison, Scenario 1 employs the optimized dwell time proposed in this paper, but the nearest three-vector solution is used as the benchmark, and Scenario 2 uses the proposed scheme. It can be observed that the computation

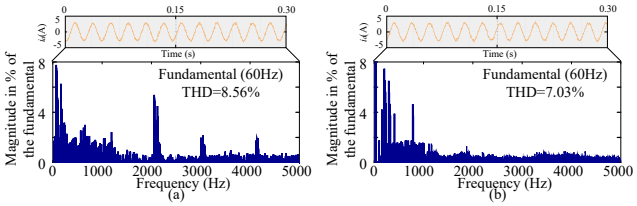

Fig. 23. Steady-state stator current curves and their FFT spectra with parameter mismatch. (a) Proposed method when inductance decreases by 50%. (b) Proposed method when flux-linkage increases by 50%.

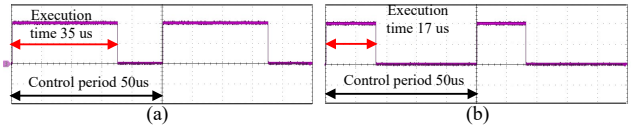

Fig. 24. Algorithm execution time comparison. (a) Scenario 1. (b) Scenario 2.

time for Scenario 1 is longer at 35.6μs. This is due to the fact that the unsimplified multi-vector algorithm needs to compute the predicted currents for the 27 switching states of the three-level inverter and traverse to find the optimal output combination. Scenario 2 is 55% faster than Scenario 1. In addition, the complete operation of the proposed scheme is tested, and 9.3μs of code execution time is required to detect the neutral current polarity and the data retention time for the hysteresis control process. The proposed method is better in terms of overall performance and is more computationally efficient. Relieving the computational burden is meaningful for practical applications, incorporate protection functions and communication. The proposed method can leave more time margin for other steps required for code implementation.

VI. Conclusion

In this paper, a novel multi-vector MPC method for 3L-NPC inverter-powered PMSM is proposed, aiming to improve computational efficiency and synergistically suppress CMV and balance NPP. In the proposed method, the optimal dwell time of each adjacent vector is calculated by the cost function without weight factors. To realize the independence of capacitor parameters and NPP balance, a hysteresis controller is introduced. The positive and negative NPP polarities of various vectors in different sub-hexagons are fully utilized to decouple vector selection from CMV suppression/NPP balance. Comparative experiments are conducted with other three-level MPC algorithms, which reveal that the proposed method have not only satisfactory steady-state output performance but also fast transient response. The effectiveness and robustness of the proposed method is also verified. The CMV is restricted within $\pm V_{dc}/6$ most of the time, and the NPP imbalance situation has also been greatly improved. Future work will focus on the multiple sampling mechanism of the three-level MPC, MPC optimization considering three-level inverter nonlinearity, and enhanced robust MPC under parameter mismatch.

References

[1] J. D. Barros, J. F. A. Silva, and E. G. A. Jesus, "Fast-predictive optimal control of NPC multilevel converters," *IEEE Trans. Ind. Electron.*, vol. 60, no. 2, pp. 619–627, Feb. 2013, doi:10.1109/TIE.2012.2206352.

[2] D. Zhou, C. Jiang, Z. Quan, and Y. R. Li, "Vector shifted model predictive power control of three-level neutral-point-clamped rectifiers," *IEEE Trans. Ind. Electron.*, vol. 67, no. 9, pp. 7157–7166, Sep. 2020, doi:10.1109/TIE.2019.2946549.

[3] Z. Xue, S. Niu, and X. Li, "A simplified multivector-based model predictive current control for PMSM with enhanced performance," *IEEE Trans. Transport. Electrific.*, vol. 9, no. 3, pp. 4032–4044, Sep. 2023, doi:10.1109/TTE.2023.3242685.

[4] Z. Wang, A. Yu, X. Li, G. Zhang, and C. Xia, "A novel current predictive control based on fuzzy algorithm for PMSM," *IEEE Trans. Emerg. Sel. Topics Power Electron.*, vol. 7, no. 2, pp. 990–1001, Jun. 2019, doi:10.1109/JESTPE.2019.2902634.

[5] S.-W. Kang, J.-H. Soh, and R.-Y. Kim, "Symmetrical three-vector-based model predictive control with deadbeat solution for IPMSM in rotating reference frame," *IEEE Trans. Ind. Electron.*, vol. 67, no. 1, pp. 159–168, Jan. 2020, doi:10.1109/TIE.2018.2890490.

[6] C. Wang and Z. Q. Zhu, "Fuzzy logic speed control of permanent magnet synchronous machine and feedback voltage ripple reduction in flux-weakening operation region," *IEEE Trans. Ind. Appl.*, vol. 56, no. 2, pp. 1505–1517, Mar./Apr. 2020, doi:10.1109/TIA.2020.2967673.

[7] T. T. Nguyen, H. N. Tran, T. H. Nguyen, and J. W. Jeon, "Recurrent neural network-based robust adaptive model predictive speed control for PMSM with parameter mismatch," *IEEE Trans. Ind. Electron.*, vol. 70, no. 6, pp. 6219–6228, Jun. 2023, doi:10.1109/TIE.2022.3198255.

[8] Z. Yin, L. Gong, C. Du, J. Liu, and Y. Zhong, "Integrated position and speed loops under sliding-mode control optimized by differential evolution algorithm for PMSM drives," *IEEE Trans. Power Electron.*, vol. 34, no. 9, pp. 8994–9005, Sep. 2019, doi:10.1109/TPEL.2018.2889781.

[9] M. Novak, U. M. Nyman, T. Dragicevic, and F. Blaabjerg, "Analytical design and performance validation of finite set MPC regulated power converters," *IEEE Trans. Ind. Electron.*, vol. 66, no. 3, pp. 2004–2014, Mar. 2019, doi:10.1109/TIE.2018.2838073.

[10] G. Liu, C. Song, and Q. Chen, "FCS-MPC-Based fault-tolerant control of five-phase IPMSM for MTPA operation," *IEEE Trans. Power Electron.*, vol. 35, no. 3, pp. 2882–2894, Mar. 2020, doi:10.1109/TPEL.2019.2931712.

[11] Y. Luo and C. Liu, "Pre- and post-fault tolerant operation of a six-phase PMSM motor using FCS-MPC without controller reconfiguration," *IEEE Trans. Veh. Technol.*, vol. 68, no. 1, pp. 254–263, Jan. 2019, doi:10.1109/TVT.2018.2883665.

[12] W. Shen, L. Shao, D. Liu, J. Wang, and C. Ge, "Event-triggered FCS-MPC with sliding mode observer for permanent magnet synchronous motor servo motion systems," *IEEE Trans. Autom. Sci. Eng.*, early access, doi:10.1109/TASE.2024.3377639.

[13] J. Rodriguez, S. Bernet, P. K. Steimer, and I. E. Lizama, "A survey on neutral-point-clamped inverters," *IEEE Trans. Ind. Electron.*, vol. 57, no. 7, pp. 2219–2230, Jul. 2010, doi:10.1109/TIE.2009.2032430.

[14] Z. Zhang, C. M. Hackl, and R. Kennel, "Computationally efficient DMPC for three-level NPC back-to-back converters in wind turbine systems with PMSG," *IEEE Trans. Power Electron.*, vol. 32, no. 10, pp. 8018–8034, Oct. 2017, doi:10.1109/TPEL.2016.2637081.

[15] X. Zhang, X. Wu, G. Tan, W. Zhang, and Q. Wang, "A dual-vector model predictive control method with minimum current THD," *IEEE Trans. Power Electron.*, vol. 36, no. 9, pp. 9758–9762, Sep. 2021, doi:10.1109/TPEL.2021.3065009.

[16] C. Xiong, H. Xu, T. Guan, and P. Zhou, "A constant switching frequency multiple-vector-based model predictive current control of five-phase PMSM with nonsinusoidal back EMF," *IEEE Trans. Ind. Electron.*, vol. 67, no. 3, pp. 1695–1707, Mar. 2020, doi:10.1109/TIE.2019.2907502.

[17] W. Alhosaini, Y. Wu, and Y. Zhao, "An enhanced model predictive control using virtual space vectors for grid-connected three-level neutral-point clamped inverters," *IEEE Trans. Energy Convers.*, vol. 34, no. 4, pp. 1963–1972, Dec. 2019, doi:10.1109/TEC.2019.2923370.

[18] F. Donoso, A. Mora, R. Cárdenas, A. Angulo, D. Sáez, and M. Rivera, "Finite-set model-predictive control strategies for a 3L-NPC inverter operating with fixed switching frequency," *IEEE Trans. Ind. Electron.*, vol. 65, no. 5, pp. 3954–3965, May 2018, doi:10.1109/TIE.2017.2760840.

[19] T. Liu, A. Chen, and Y. Huang, "Multivector model predictive current control for paralleled three-level t-type inverters with circulating current

elimination," *IEEE Trans. Ind. Electron.*, vol. 70, no. 8, pp. 8042–8052, Aug. 2023, doi:10.1109/TIE.2022.3208607.

[20] Y. Yang, H. Wen, M. Fan, X. Zhang, L. He, R. Chen, M. Xie, M. Norambuena, and J. Rodriguez, "Low complexity finite-control-set MPC based on discrete space vector modulation for t-type three-phase three-level converters," *IEEE Trans. Power Electron.*, vol. 37, no. 1, pp. 392–403, Jan. 2022, doi:10.1109/TPEL.2021.3098661.

[21] X. Song, H. Wang, X. Ma, X. Yuan, and X. Wu, "Robust model predictive current control for a nine-phase open-end winding PMSM with high computational efficiency," *IEEE Trans. Power Electron.*, vol. 38, no. 11, pp. 13 933–13 943, Nov. 2023, doi:10.1109/TPEL.2023.3309308.

[22] Y. Yang, H. Wen, M. Fan, M. Xie, and R. Chen, "Fast finite-switching-state model predictive control method without weighting factors for t-type three-level three-phase inverters," *IEEE Trans. Ind. Informat.*, vol. 15, no. 3, pp. 1298–1310, Mar. 2019, doi:110.1109/TII.2018.2815035.

[23] Y. Yang, H. Wen, R. Chen, M. Fan, X. Zhang, M. Norambuena, and J. Rodriguez, "An efficient model predictive control using virtual voltage vectors for three-phase three-level converters with constant switching frequency," *IEEE Trans. Ind. Electron.*, vol. 69, no. 4, pp. 3998–4009, Apr. 2022, doi:10.1109/TIE.2021.3075890.

[24] D. Zhou, L. Ding, and Y. R. Li, "Two-stage model predictive control of neutral-point-clamped inverter-fed permanent-magnet synchronous motor drives under balanced and unbalanced DC links," *IEEE Trans. Ind. Electron.*, vol. 68, no. 5, pp. 3750–3759, May 2021, doi:10.1109/TIE.2020.2984421.

[25] C. Qin, C. Zhang, A. Chen, X. Xing, and G. Zhang, "A space vector modulation scheme of the quasi-z-source three-level t-type inverter for common-mode voltage reduction," *IEEE Trans. Ind. Electron.*, vol. 65, no. 10, pp. 8340–8350, Oct. 2018, doi:10.1109/TIE.2018.2798611.

[26] S. Kwak and S. Mun, "Common-mode voltage mitigation with a predictive control method considering dead time effects of three-phase voltage source inverters," *IET Power Electron.*, vol. 8, no. 9, pp. 1690–1700, Sep. 2014, doi:10.1049/iet-pel.2014.0884.

[27] F. Guo, A. M. Diab, S. S. Yeoh, T. Yang, S. Bozhko, P. Wheeler, and Y. Zhao, "An advanced dual-carrier-based multi-optimized PWM strategy of three-level neutral-point-clamped converters for more-electric-aircraft applications," *IEEE Trans. Energy Convers.*, vol. 39, no. 1, pp. 356–367, Mar. 2024, doi:10.1109/TEC.2023.3312599.

[28] P. Liu, S. Duan, C. Yao, and C. Chen, "A double modulation wave CBPWM strategy providing neutral-point voltage oscillation elimination and CMV reduction for three-level NPC inverters," *IEEE Trans. Ind. Electron.*, vol. 65, no. 1, pp. 16–26, Jan. 2018, doi:10.1109/TIE.2017.2723866.

[29] H. Yang, Y. Zhang, and M. Li, "Duty-cycle correction-based model predictive current control for PMSM drives fed by a three-level inverter with low switching frequency," *IEEE Trans. Power Electron.*, vol. 38, no. 6, pp. 6841–6850, Jun. 2023, doi:10.1109/TPEL.2023.3250480.

[30] Y. Zhang, Y. Bai, H. Yang, and B. Zhang, "Low switching frequency model predictive control of three-level inverter-fed IM drives with speed-sensorless and field-weakening operations," *IEEE Trans. Ind. Electron.*, vol. 66, no. 6, pp. 4262–4272, Jun. 2019, doi:10.1109/TIE.2018.2868014.

[31] X. Wang, J. Zou, L. Ma, J. Zhao, C. Xie, K. Li, L. Meng, and J. M. Guerrero, "Model predictive control methods of leakage current elimination for a three-level t-type transformerless PV inverter," *IET Power Electron.*, vol. 11, no. 8, pp. 1492–1498, Jul. 2018, doi:10.1049/iet-pel.2017.0762.

[32] C. Zhang, C. Gan, K. Ni, S. Wang, J. Sun, Z. Yu, and R. Qu, "Model-free predictive voltage control of the floating capacitor in hybrid-inverter open- winding permanent magnet synchronous motor," *IEEE Trans. Ind. Electron.*, vol. 71, no. 10, pp. 11 925–11 935, Oct. 2024, doi:10.1109/TIE.2024.3355487.

[33] S. Wang, Y. Zhang, Q. Zhang, J. Zhao, and Q. Zhang, "Model predictive torque control for dual three-phase PMSM based on novel virtual voltage vector," *IEEE Trans. Energy Convers.*, vol. 39, no. 3, pp. 1488–1496, Sep. 2024, doi:10.1109/TEC.2024.3366182.

[34] F. Guo, T. Yang, A. M. Diab, S. S. Yeoh, S. Bozhko, and P. Wheeler, "An enhanced virtual space vector modulation scheme of three-level NPC converters for more-electric-aircraft applications," *IEEE Trans. Ind. Appl.*, vol. 57, no. 5, pp. 5239–5251, Sep./Oct. 2021, doi:10.1109/TIA.2021.3085798.

[35] A. R. Beig, G. Narayanan, and V. T. Ranganathan, "Modified svpwm algorithm for three level vsi with synchronized and symmetrical waveforms," *IEEE Trans. Ind. Appl.*, vol. 54, no. 1, pp. 486–494, Feb. 2007, doi:10.1109/TIE.2006.888801.